Progress in Additive Manufacturing (2023) 9:1843–1856
https://doi.org/10.1007/s40964-023-00547-z

FULL RESEARCH ARTICLE

Atomized scrap powder feedstock for sustainable Inconel 718 additive manufacturing via LPBF: a study of static and fatigue properties

M. Benedetti[1] · M. Perini[2] · M. Vanazzi[3] · A. Giorgini[3] · G. Macoretta[4] · C. Menapace[1]

Received: 5 June 2023 / Accepted: 17 November 2023 / Published online: 11 December 2023

Abstract

Inconel 718 is a popular superalloy with high strength and corrosion-resistance properties that make it widely used in aerospace and nuclear industries. The conventional production of Inconel 718 powder feedstock involves a considerable amount of energy consumption and greenhouse gas emissions. This study investigates the feasibility of using atomized metallic scrap to produce Inconel 718 powder feedstock, as a more sustainable alternative. Life cycle assessments showed that this approach reduces carbon footprint and energy consumption by more than 90% compared to conventional production methods. The study also carried out comparative microstructural, static and fatigue analyses to address concerns about potential impurities in the secondary-source powder feedstock. The results indicate that this secondary-source powder feedstock can achieve properties comparable to those of conventionally processed powders, with negligible loss in ductility and fatigue strength, without requiring ad-hoc tuning of the LPBF process parameters. Overall, the findings suggest that using Inconel 718 powder feedstock produced from secondary sources can be a promising and sustainable alternative to conventional production methods.

Keywords Circular economy · Secondary raw materials · Inconel 718 · Laser powder bed fusion · Fatigue · Tensile properties

1 Introduction

According to recent trends in the manufacturing process, components made of conventional metals such as steel and aluminum exhibit scrap percentages of approximately 15% to 20%, while those made of titanium and nickel alloys, commonly used in the aerospace and energy sectors, show scrap percentages of approximately 40% to 50% [1]. Consequently, reducing scrap production and reusing any inevitable scrap, particularly in the case of alloys containing critical raw materials such as Ti and Ni, is of paramount importance.

With the development of regulations, the traditional linear economy of the manufacturing process is being replaced by a circular economy that emphasizes recycling and reuse. The two primary contributors to recycling and reuse in the metallic industry are the actual product at the end of its life and the metallic waste/scrap generated during subtractive manufacturing processes. Additive manufacturing, being a near net shape technology, is an effective route to reduce this second source of waste. Virgin powders for the additive manufacturing process are produced using atomization techniques to obtain spherical powder particles from primary metallic billets. However, there is increasing interest in producing powder feedstock from secondary resources by subjecting metallic waste to gas, plasma, and water atomization or mechanical milling [2–4]. Some life cycle assessment (LCA) studies have demonstrated that producing powder feedstock through scrap atomization leads to a more sustainable AM process with a reduction in cost and carbon footprint [5].

Despite the undeniable advantages of using recycled powders from an environmental and raw material supply standpoint, the industry still harbors mistrust regarding

✉ M. Benedetti
matteo.benedetti@unitn.it

1 Department of Industrial Engineering, University of Trento, Trento, Italy

2 ProM Facility, Trentino Sviluppo S.P.a., Rovereto, Italy

3 F3nice, Piantedo, Italy

4 Department of Civil and Industrial Engineering, University of Pisa, Pisa, Italy

the widespread use of such powders in critically loaded mechanical components. There is a need for solid answers and guidance regarding this matter. The accumulation of impurities in metal powders used in additive manufacturing is a significant concern as it can render them unsuitable for direct use, necessitating costly and time-consuming purification processes. Metal scrap can come into direct contact with machine tools, oil, reactive gases, moisture, improper disposal, and incorrect sorting, all of which can alter the powder's chemical composition and/or adversely affect its performance. Traceability is crucial during the recycling process, particularly in industries such as aerospace and biomedical, where quality control and standardization are critical. This is necessary to monitor the potential contamination level of the feedstock. Powder flowability is another concern, as it depends on chemical composition, powder morphology and size distribution that can be different in recycled powders with respect to conventional ones [6, 7]. To this regard, a sort of deterioration in mechanical properties was observed when employing recycled powder in additive manufacturing processes [8–10]. Recently, Tupac-Yupanqui and Armani [11] fabricated laboratory samples of Inconel 718 using metal additive manufacturing, employing a powder feedstock derived from the recycling and melting of used parts. While their study did not detect any deterioration in quasi-static mechanical properties, they did not investigate fatigue properties, which are typically more susceptible to the effects of potential contaminations.

The objective of this study is to evaluate the challenges associated with utilizing powder feedstocks sourced from secondary materials in the production of Inconel 718 alloy. To achieve this, we conducted a comparative analysis between conventionally processed powder and an innovative powder generated through the atomization of metallic scrap. In Sect. 2, we will outline the methodologies employed for the fabrication and characterization of these powder feedstocks, considering both their environmental and mechanical aspects. Section 3 will present the outcomes of a comprehensive Life Cycle Assessment (LCA) analysis, highlighting the environmental and energy-related advantages offered by the latter powder source. In addition, we will present the results of static and fatigue characterizations carried out on laboratory samples manufactured through laser powder bed fusion (LPBF) using both types of powder feedstocks. Finally, in Sect. 4, we will provide concluding remarks and offer insights into potential avenues for future research in this field.

2 Materials and experimental procedures

Figure 1 schematically illustrates the main steps involved in a conventional (Fig. 1a) and new (Fig. 1b) production process of Inconel 718 powder feedstock. The new process (hereinafter denoted as "Atomized scrap (AS)") involves different pretreatments for bulky scrap and exhausted powder, respectively, and all the scrap metal is obtained burden-free from its source. The bulky scrap fraction is properly selected, and its geometry and composition optimized to guarantee an adequate quality level of the feedstock produced. Specifically, 75% of the bulky scrap must be cut due to the limitations of the atomizer's crucible, followed by an intensive cleaning process in an ultrasonic cleaning machine with the addition of a cleaning agent. The scrap contains

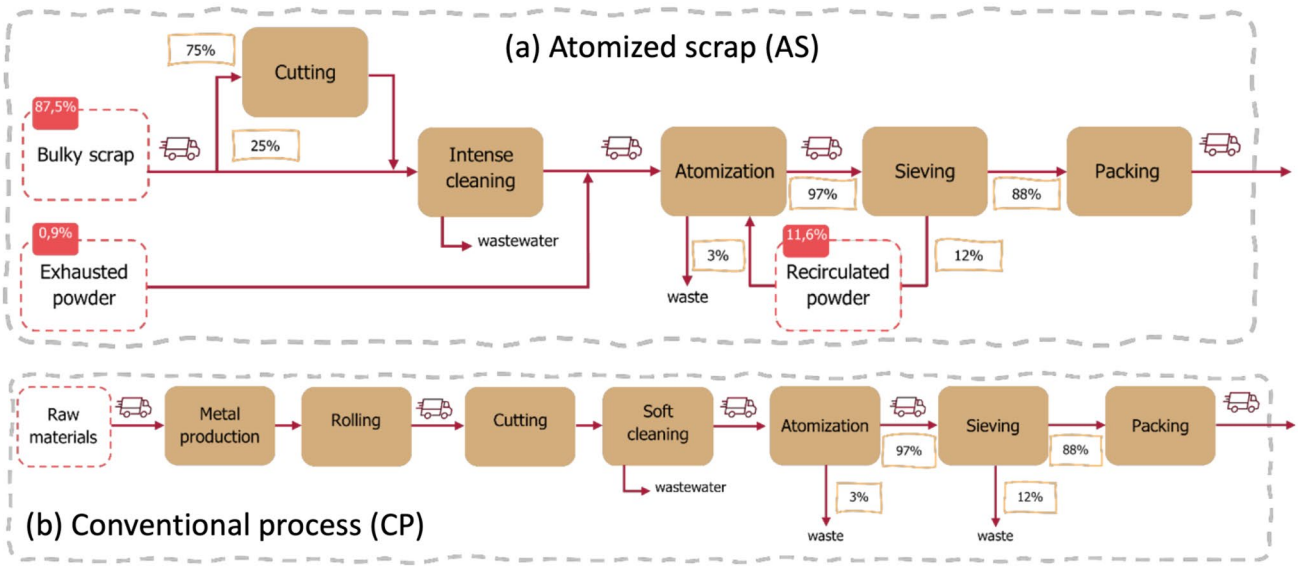

Fig. 1 AM powder production process. **a** Innovative from atomized scrap, **b** conventional

12.5 wt. % of powders from two sources, including the recirculated powder from the sieve and an external source of exhausted powder. This second group can also include powders recovered from the additive manufacturing (AM) production, i.e., the powders that are non-sintered/melted and left in the AM chamber. Atomization is then performed by vacuum induction-melting inert gas atomization (VIGA) technology.

In contrast, the conventional process (CP) depicted in Fig. 1a involves Inconel production as the first step, followed by rolling to produce bars, cutting of the bars to the proper dimensions required by the atomizer, atomization, sieving, and packing. In the first process, there is a 12% loss of material in the sieving unit and a 3% loss in the atomizer. In the present work, CP powder of Inconel 718–0405 alloy was produced by VIGA and supplied by Renishaw, featuring a chemical composition compliant with the ASTM F3055 standard.

To evaluate the environmental impact of the two powder production routes shown in Fig. 1a and b, we used two methods: the Environmental Product Declaration (EPD) 2018 [12] and the Cumulative Energy Demand (CED) [13]. The EPD is a standardized instrument based on the quantification of the environmental impacts associated with the product throughout its life cycle. Based on a comprehensive LCA analysis (cradle-to-grave), EPDs include information on environmental performance at every stage of the life cycle, from raw material acquisition to the use of energy and material resources. In Europe, all EPDs must conform to European standard EN 15804 EPD, and all EPDs report the same list of environmental impact indicators, making it easy to compare multiple products. The 25 indicators are grouped by Environmental Impact, Resource use, and Output flows and waste categories. The CED method (also called "primary energy consumption") represents the direct and indirect energy use throughout the life cycle, including the energy consumed during the extraction, manufacturing, and disposal of the raw and auxiliary materials. It is frequently used as a screening impact indicator.

To evaluate the mechanical performances, laboratory specimens were produced using a Concept Laser Mlab Cusing, characterized by a 100 W laser and a 50 µm focal diameter, installed in the laboratory of ProM facility (Rovereto, Italy). The laser beam modulation parameters were set to have a continuous wave emission. Specifically, cylindrical bars (10 mm diameter) were built in an Ar protective atmosphere along the vertical direction, namely with the longitudinal direction orthogonal to the building platform.

The process parameters were the same for both powder feedstocks and are listed in Table 1 (where P is the laser power, v the scanning speed, h the hatch distance, and t the layer thickness) and were set according to an optimization strategy internally carried out by ProM on conventional powder feedstocks. This strategy included a Design of Experiments (DOE) approach, wherein 12 cubic samples were produced under the same laser power setting ($P = 90$ W). This DOE exploration encompassed three different laser scan speeds (v) at 600, 750, and 900 mm/s, along with four hatch distances (h) at 55, 66, 77, and 88 µm. The optimal parameter set listed in Table 1 led to the highest relative density, which was measured with the Archimedes' method equal to 99.8%.

Table 1 Process parameters of the LPBF adopted for CP and AS powder feedstocks

Laser power, P (W)	Scan speed, v (mm/s)	Hatch distance, h (µm)	Layer thickness, t (µm)	Energy density, E_d (J/mm^3)	Scanning strategy
90	750	77	25	62.3	Meander

Table 1 reports also the energy density E_d expressed by [14]

$$E_d = \frac{P}{v \bullet h \bullet t} \quad (1)$$

Interestingly, the energy density resulting from the optimized process parameters set turned out to lie in the safe region not affected by keyhole and lack of fusion according to the investigations done in [14]. Similar optimal E_d values, exceeding 60 J/mm^3, were also reported in [11].

The printed cylindrical bars were subjected to an aging heat treatment according to AMS 5663 standard [15]. The rationale behind this choice was to investigate the possible effect of impurities in the AS powder feedstock in the most unfavorable conditions possible, viz. under aged microstructural conditions that lead to high tensile properties accompanied by a remarkable ductility loss with respect to the as-built condition [14]. Specifically, the heat treatment is composed of solution treatment (980 °C, 1 h) followed by a furnace forced cooling to 50 °C at 100 °C/and a double aging (720 °C, 8 h; furnace cooling at 55 °C/h to 620 °C, 8 h/air cooling).

After heat treatment, the cylindrical bars were turned to fabricate dog-bone specimens for quasi-static tensile (Fig. 2a) and axial fatigue tests (Fig. 2b), respectively. The formers have a gauge diameter of 4 mm and are compliant with the ASTM E8-16 standard. The latter have been designed according to ASTM E466 standard and feature a uniform 4 mm diameter along the gauge length. In this way, a significant amount of material is critically stressed, so that the impact of microstructure and defectiveness on the fatigue behavior can be captured more effectively compared to common hourglass specimens [16]. The surface roughness was measured using a contact profilometer having a stylus with tip radius of 2 µm. A cutoff distance of 2.5 mm along the

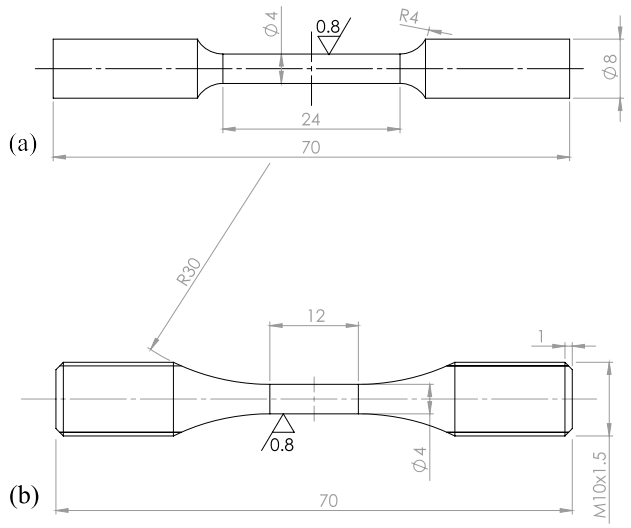

Fig. 2 Specimens geometry. **a** Quasi-static tests, **b** axial fatigue tests. Dimensions in mm

Table 2 Surface roughness measurement. Average and standard deviation based on three replicated measures

Powder feedstock	Ra (μm)	RzISO (μm)	Rt (μm)	Rq (μm)
CP	0.5 ± 0.1	3.5 ± 0.6	4.5 ± 0.7	0.7 ± 0.1
AS	0.6 ± 0.1	3.4 ± 0.1	4.3 ± 0.4	0.7 ± 0.0

specimens' longitudinal direction was selected according to ISO standard 4288:1998. The results are listed in Table 2. The surface finish was comparable for samples manufactured using both powders and is sufficiently smooth to rule out any significant impact on the quasi-static and fatigue properties of the samples, which is rather dictated by internal defectiveness, as discussed in the following.

Monotonic tensile tests (initial strain rate of 1×10^{-4} s^{-1}) were performed at room temperature (25 °C, 60% relative humidity) using a servo-hydraulic universal testing machine INSTRON 1343 equipped with hydraulic grips, a load cell of 100 kN (non- linearity ± 0.1% of rated output R.O.) and an axial extensometer (10 mm gage length, nonlinearity ± 0.15% of R.O.). Five tests were replicated for each experimental condition. The yield strength was determined as the 0.2% offset yield stress.

To evaluate the high-cycle-fatigue (HCF) behavior, axial fatigue tests were conducted in laboratory environment using a resonant testing machine Rumul Mikrotron 20 kN operating at a nominal frequency of 150 Hz under load control and stress ratio $R = 0.1$. Tests were carried out at different stress amplitudes to explore fatigue lives comprised between 10^5 and 3×10^7 cycles. The S–N curve for each experimental condition was obtained from 15 samples. Run-out tests were terminated at 3×10^7 cycles when no facture took place.

The S–N curve were fitted by the following power-law equation enriched with a constant term to better represent their asymptotic behavior [17]:

$$\sigma_a = c_1 + \frac{c_2}{N_f^{c_3}} \tag{2}$$

The scatter of the fatigue data was assessed by computing the estimated regression variance assumed to be uniform for the whole fatigue life range and expressed by

$$S^2 = \frac{\sum_{i=1}^{n} \left(\sigma_{a,i} - \hat{\sigma}_{a,i}\right)^2}{n - p} \tag{3}$$

where $\sigma_{a,i}$ is the i-th fatigue amplitude data point, $\hat{\sigma}_{a,i}$ is its estimator, n is the number of data elements, and p is the number of parameters in the regression ($p = 3$).

Metallographic samples were prepared according to the standard procedure (hot mounting in resin, grinding and polishing). Etching was performed with Kalling 2 reagent (100 ml Ethanol, 100 ml HCl, 5 g $CuCl_2$), applied for 30 s. To examine the microstructure of both the tensile and fatigue samples in the cross-section perpendicular to the building direction, optical microscopy was employed using a Zeiss Axiophot microscope. Furthermore, scanning electron microscopy (SEM) was conducted using a Jeol IT 300 electron microscope equipped with an energy-dispersive X-ray spectroscopy (EDXS) system. The SEM analysis also extended to the fracture surfaces of both the tensile and fatigue samples. Unetched metallographic sections were prepared specifically for characterizing the morphology of pores using Image Analysis software, namely Image J. The analysis of porosity involved examining various transversal sections to obtain a statistically significant number of pores, amounting to approximately 500. Pore shape factor f_s was evaluated according to this formula:

$$f_s = \frac{4\pi A}{P^2} \tag{4}$$

where A and P are the pore area and perimeter, respectively. $f_s = 1$ corresponds to a perfectly circular shape.

The SEM fractographic analyses done on all the fatigued specimens were used to reanalyze the SN fatigue data according to a fracture mechanics approach. Specifically, the stress intensity factor range (ΔK) for each killer pore was assessed using the following formula [18]:

$$\Delta K = Y \bullet \Delta\sigma \bullet \sqrt{\pi\sqrt{area}} \tag{5}$$

where Y is the shape factor ($Y = 0.50$ for internal defects and $Y = 0.65$ for surface defects [18, 19]) and $\Delta\sigma = 2\sigma_a$ is

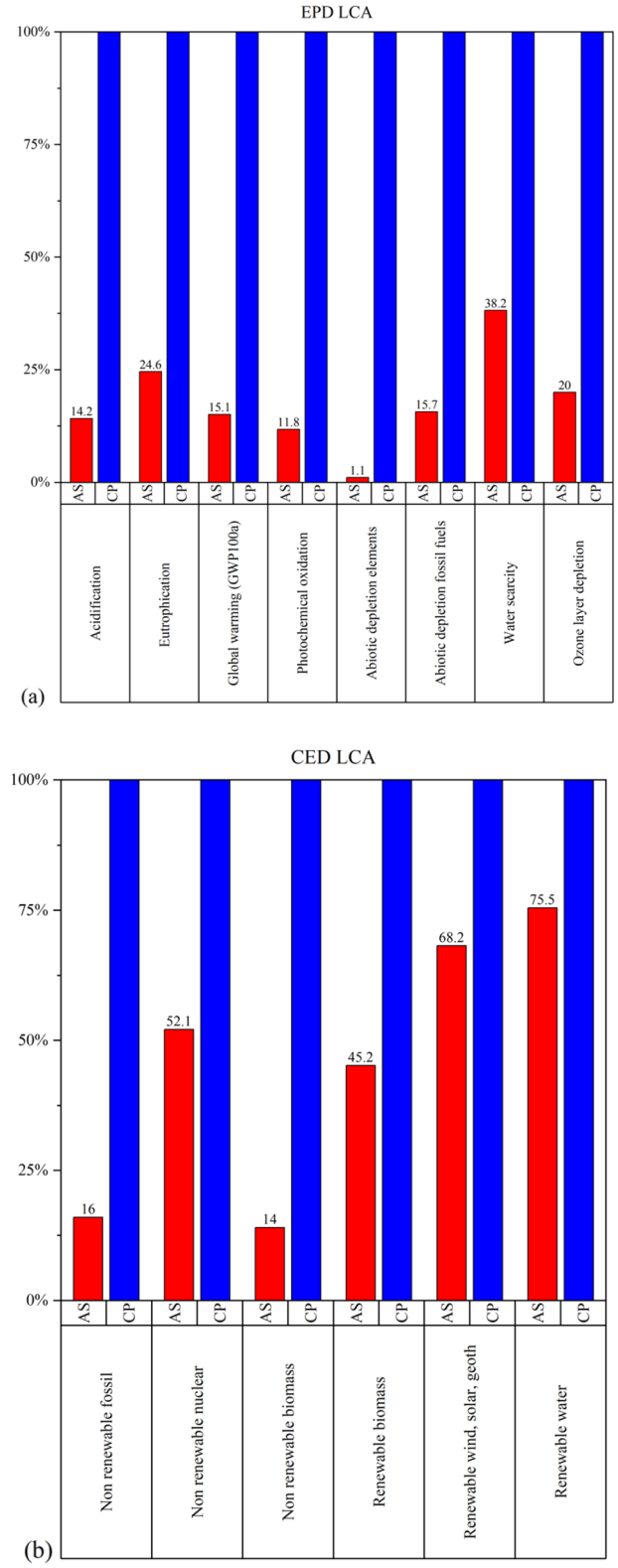

Fig. 3 Relative results of the comparative analysis of conventional (CP) and innovative process (AS). **a** EPD 2018 method, **b** CED method

the stress range at which the fatigue specimen was tested. A Basquin power-law has been used to fit the ΔK vs N_f data:

$$\Delta K = \frac{k_1}{N_f^{k_2}} \tag{6}$$

The standard deviation was assessed using a formula similar to Eq. (3).

Microhardness measurements were carried out on metallographic surfaces with the help of a Vickers micro-indenter, by applying a load of 25 gr (HV0.025). Ten measurements for each sample were averaged.

The obtained static and fatigue results were compared with those obtained under similar testing conditions (machined surfaces, aged microstructure) using a Renishaw RenAM 500S Flex LPBF printing machine operating at the University of Pisa (Italy) with process parameters tuned in [14] resulting in an energy density $E_d = 57.6$ J/mm^3, thus very similar to that adopted in the present work. The specimens present a gauge diameter of 6 mm and surface roughness similar to the CP and AS samples. The static and fatigue testing strategy was the same as that described in [14]. This material variant will be denoted in the following as Control Batch (CB).

3 Results and discussion

3.1 Life cycle assessment

Figure 3 compares the environmental impacts of the two powder production routes. Importantly, the new process (AS) has lower impacts for all the impact categories

Table 3 Chemical composition (oxygen included) of the two powders

Element	CP %wt	AS %wt
O	0.011	0.009
Ni	54.9	54.5
Cr	18.2	18.6
Cu	0.01	0.05
Nb	4.80	4.95
Mo	2.95	3.03
Ti	0.93	0.93
Al	0.44	0.45
Co	0.12	0.05
C	0.05	0.03
Mn	0.01	0.09
Si	< 0.05	0.11
P	0.010	0.007
S	0.003	< 0.003
Fe	17.2	17.1

considered, both for the evaluations using the EPD 2018 (Fig. 3a) and the CED (Fig. 3b) methods, respectively. In particular, the results of LCA with the EPD 2018 method for the conventional process show that the main impact is due to Inconel production, followed by atomization. In the global warming category, the impact is reduced by 92.85% by replacing the conventional process with the new one. The main reason for this reduction is the elimination of Inconel billets production and the use of just scrap Inconel instead of them. The results obtained from the CED method (Fig. 3b) show analogously that Inconel production is the dominant hotspot, along with a relevant contribution from atomization in the categories "Non-renewable, nuclear" and "Renewable, wind, solar, geothermal".

The AS process has significantly reduced the environmental impact parameters compared to CP. This is mainly due to the utilization of metallic scrap instead of virgin material bars, which directly benefits the reduction of emissions throughout the entire production process. This outcome is quite challenging from a circular economy perspective. The metallic waste used as raw materials in the new production process would have had a much greater environmental impact if they had not been collected, sorted, and reused. One of the most significant impact indices of the new process is its global warming category. The environmental impact of producing 10 kg of powder using the new process results in 10.86 kg CO_{2eq}. In addition, the energy demand of the new process falls under the "Non-renewable, fossil" category, with a production burden of 129.68 MJ per 10 kg of powder produced. In comparison, the conventional process results in much higher CO_{2eq} and embodied energy values. For 10 kg of powder produced, the CO_{2eq} and embodied energy values

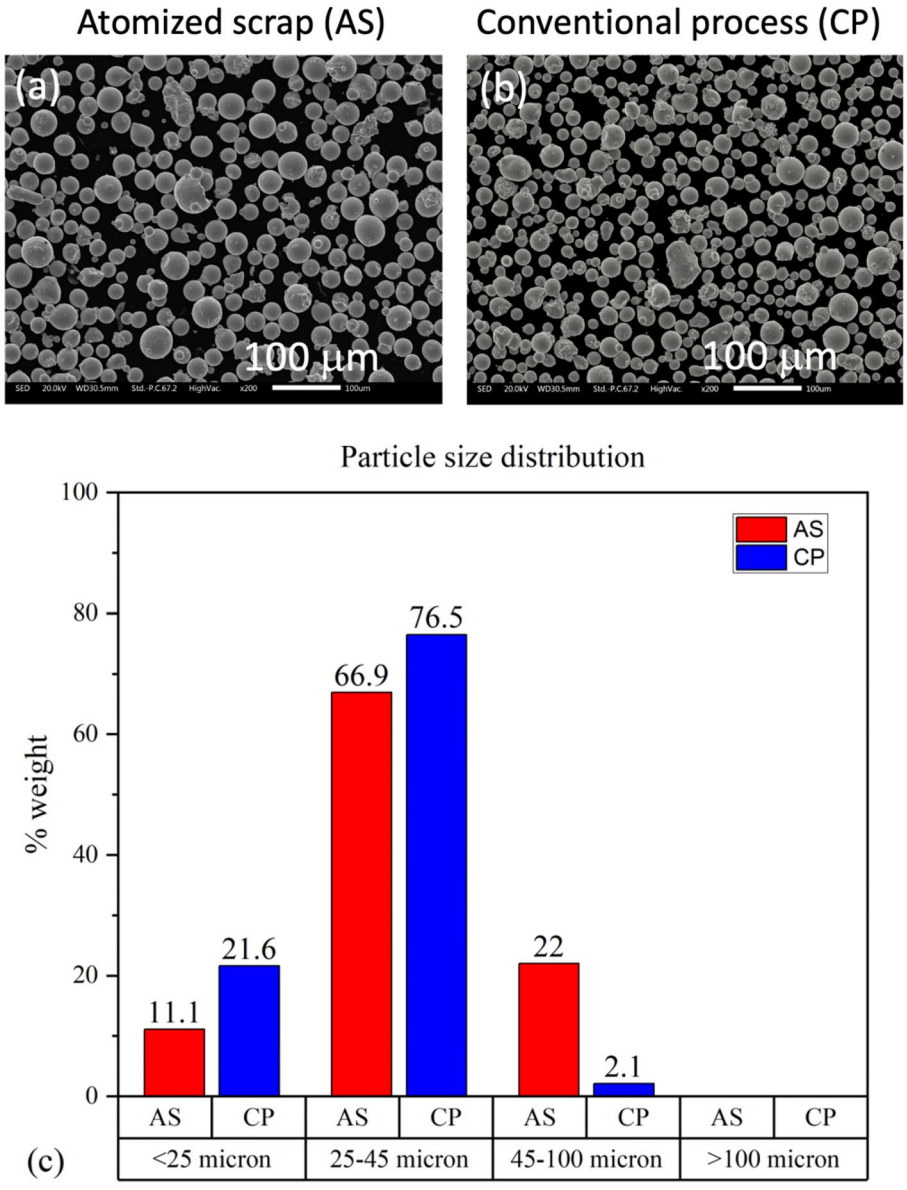

Fig. 4 Powder morphology (**a** atomized scrap, **b** conventional process) and size distribution (**c**)

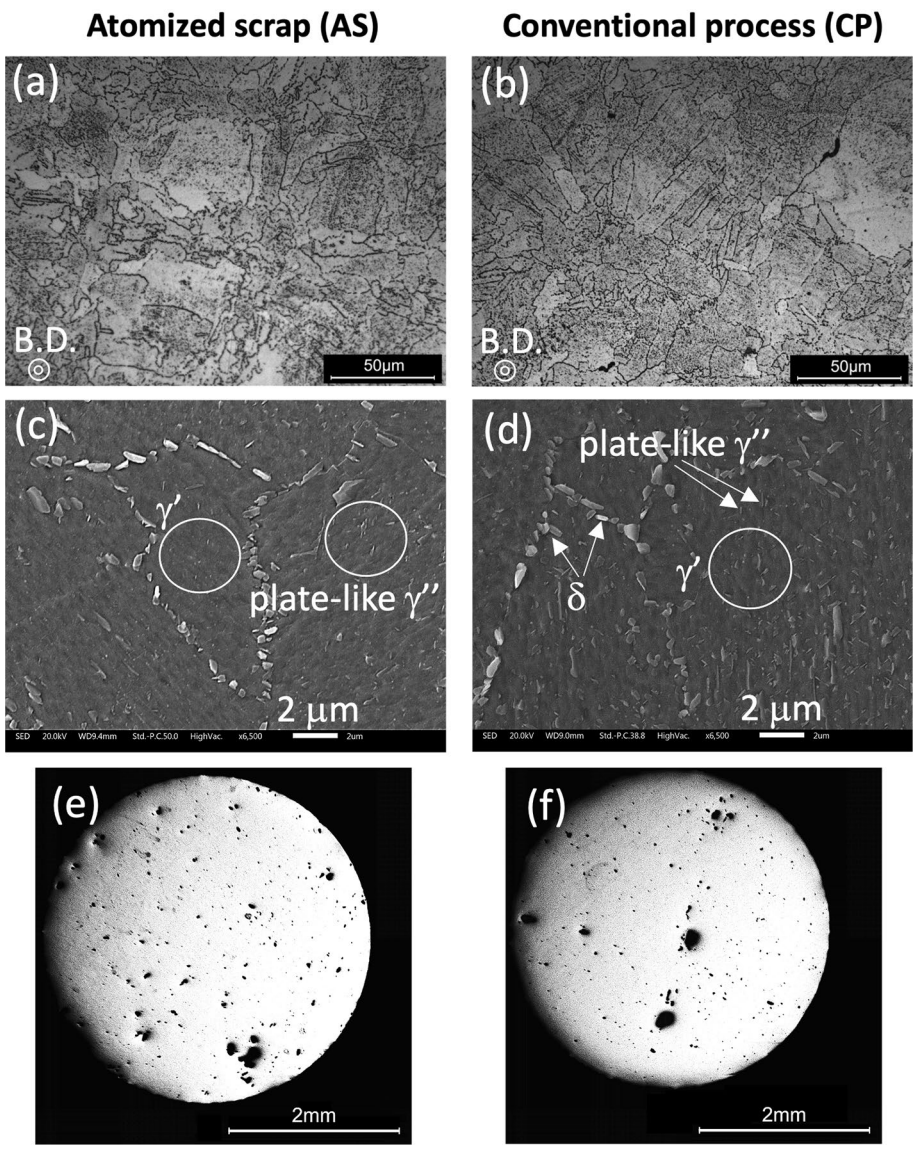

Fig. 5 **a**, **b** Light optical micrographs of the microstructure on transversal cross-section ("B.D." denotes the building direction). **c**, **d** SEM micrograph showing the fine dispersion of precipitates. (**e**, **f**) Transversal cross-section showing internal porosity. (**a**–**c**–**e**) atomized scrap, (**b**–**d**–**f**) conventional process

for the categories "Global warming" and "Non-renewable, fossil" are 151.91 kg CO_{2eq} and 1991.33 MJ, respectively. It is evident that the production of new powder by recycling general scrap and wasted powders after one or more AM cycles requires significantly less energy than fabricating powder from raw materials. The embodied energy is reduced since the most expensive primary production step, which is the production of the alloy from raw materials, is not necessary. In addition, the reduction in CO_2 emissions provides a significant advantage for sustainability.

3.2 Powders chemical composition and morphology

The chemical composition of both powder feedstocks, as determined according to the standard ASTM E1019-18/ ASTM E2594-20, is presented in Table 3. Specifically, the oxygen content reported in the first line of the table was determined using the Oxygen Analyzer Eltra Elementrac ONH. Remarkably, both powders exhibit a very low oxygen content, which is nearly equivalent and significantly below the required quality specification content outlined in the ASTM F3055 standard (O < 0.03%wt.). This remarkably low oxidation level of the powders minimizes issue s during the deposition process, such as gas porosity, and ensures superior metallurgical quality in the produced samples. Consequently, the manufactured samples exhibit enhanced toughness and ductility [20–22]. It is worth noting that excessive uptake of oxygen (O_2) has been identified as a restricting factor for the recyclability of powders in the LPBF process.

Figure 4a and b illustrates the morphology of powders CP and AS, respectively, and also displays their particle size distribution, which was determined through Sieve Analysis (Fig. 4c). Both powders exhibit a spherical morphology characteristic of gas atomization, with smooth particle

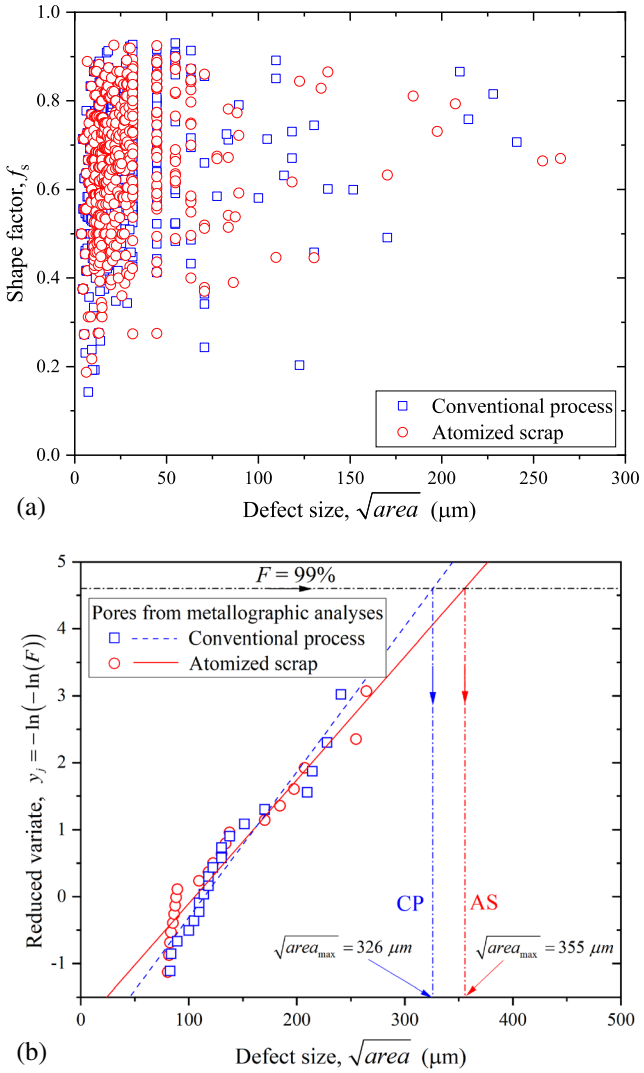

Fig. 6 Porosity characterization from image analysis of transversal cross-sections. **a** Shape factor vs. defect size. **b** Cumulative probability distributions of defect size

surfaces. Some satellites and irregularly shaped particles are observable in both powder feedstocks. The particle size distribution of AS powder is larger compared to CP powder, with a significantly higher proportion of particles falling within the 45–100 μm range (22%wt. versus 2.1%wt.).

3.3 Microstructure and defectiveness

Figure 5a and b displays the cross-sectional microstructures of CP and AS tensile samples, with "B.D." denoting the building direction. These images reveal that the fundamental microstructural characteristics of the alloy, such as grain size and shape, remain unaffected by the choice of powder. Both alloys exhibit similar features, characterized by anisotropic grains with larger dimensions parallel to the build direction, as well as the presence of some twinned grains.

Further SEM analysis in both cases unveils a fine distribution of precipitates, as depicted in Fig. 5c and d. According to investigations documented in existing literature, three primary types of precipitates are typically recognized: δ-Ni3Nb, situated at the grain boundaries; very fine cubic γ′-Ni3Al and Ni3Ti; and fine plate-like γ″-Ni3Nb, coherently dispersed within the grains [23–27]. In addition, as indicated by such research findings, it is possible that Laves phases (Ni, Fe, Cr)2(Nb, Mo, Ti) and carbides (Nb, Ti)C, initially present at the grain boundaries, dissolve after the solution + aging treatment. The aim of this precipitation hardening process is to maximize the formation of reinforcing γ′ and γ″ phases, which are coherently dispersed within the austenitic matrix, while simultaneously minimizing the presence of δ and Laves phases at the grain boundaries. This strategic approach is adopted to enhance material toughness, as the existence of δ and Laves phases can have a detrimental effect, potentially leading to intergranular fracture.

Another characteristic feature observed in the microstructure of powder-based AM Inconel 718 is the presence of porosity. Figure 5e and f presents the unetched sections of CP and AS tensile samples, revealing the presence of circular-shaped pores. These pores typically originate from entrapped gas during the molten metal stage. Notably, there is no discernible difference in the quantity, size, or shape of the pores between the two materials. To gain further insights into the pore size and shape distribution, the porosity was evaluated through image analysis of metallographic cross-sections. Figure 6a plots the shape factor f_s as a function of

Table 4 Monotonic tensile properties and hardness based on four replicated tests per material variant

Powder feedstock	*E* (GPa)	σ_Y (MPa)	σ_U (MPa)	*T.E.* (%)	*U.E.* (%)	$HV_{0.1}$
CP	178 ± 2	1250 ± 5	1440 ± 5	11.2 ± 1.0	7.6 ± 0.8	511 ± 17
AS	179 ± 2	1230 ± 5	1415 ± 5	10.6 ± 1.0	8.0 ± 1.2	501 ± 13
CB	155 ± 5	1100 ± 10	1350 ± 15	15 ± 2	15 ± 2	456 ± 2

Note: Standard error corresponds to 1σ uncertainty band

E Young's modulus; σ_U, ultimate tensile strength; σ_Y, 0.2% yield stress; *T.E.* total elongation; *U.E.* uniform elongation

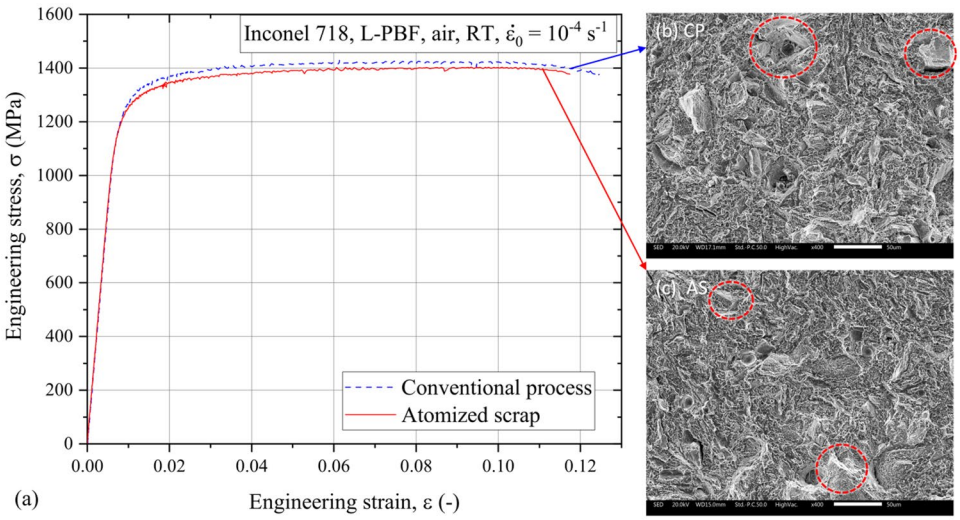

Fig. 7 **a** Representative tensile curves. SEM micrographs of the fracture surface of tensile specimens made with CP (**b**) and AS (**c**) powder feedstock. Red dashed circles denote regions of intergranular fracture

the $\sqrt{area}$ of each detected pore. It can be noted that the distributions of pore shape and size are very similar for the samples additively manufactured with the two powder types. The largest pores have a $\sqrt{area}$ of about 250 µm and a f_s value of about 0.7. This value suggests a relatively regular shape, which is more indicative of gas or keyhole porosity rather than lack of fusion defects [28, 29]. It is important to note that keyhole porosity can likely be ruled out due to the selection of an appropriate energy density that should effectively prevent their formation. On the other hand, the presence of relatively large pores, presumably containing gas, remains a plausible but not fully explained phenomenon. This aspect warrants further investigation in future research endeavors. Nevertheless, it is noteworthy that, given the similar porosity observed in both variants, its occurrence can be attributed to a minimal extent, if at all, to the use of AS powder feedstock.

Given the crucial role exerted by porosity in dictating the mechanical performances, the results of pores analyses were elaborated with the aim of estimating the expected maximum defect size $\sqrt{area}_{max}$ according to the statistics of largest extreme value distribution (LEVD) using the Maximum Likelihood Method [30, 31]. Figure 6b shows the statistical distribution of defect sizes detected in samples additively manufactured using the two powder feedstocks. Very importantly, the two distributions turned out to be very similar, leading to a maximum expected defect size with cumulative probability of 99% only slightly larger in the AS variant.

3.4 Quasi-static tensile and hardness tests

The results of the quasi-static tensile tests and hardness are listed in Table 4. Representative stress–strain curves are reported in Fig. 7a. The obtained values are in line with values reported in the literature for the same alloy in the same microstructural condition [14, 32]. The two powder feedstocks display the same ductility (expressed both in terms of uniform and total elongation). The only difference is a slightly higher strength and hardness displayed by the CP variant and a slightly lower value of total elongation in the AS condition. The presence of porosity on the fracture surface is confirmed by fractographic inspections reported in Fig. 7b and c, for CP and AS conditions, respectively. Nonetheless, a substantial portion of these fracture surfaces exhibits dimples, signifying a predominant ductile behavior, which is quite similar in both variants owing to their closely matched oxygen content. In addition, both variants display a comparable, minor fraction of intergranular fracture areas, with specific instances highlighted in Fig. 7b and c by red dashed circles. These occurrences can be attributed to a reduction in grain boundary strength, particularly in regions where a substantial precipitation of the δ phase is present. Literature data further support the notion that intergranular fracture is a potential outcome in this alloy when the cohesion along grain boundaries is compromised by the presence of precipitates [33].

Slightly different quasi-static properties are displayed by the CB, namely slightly lower strength accompanied by a higher total elongation, presumably to the different process parameters of the furnace adopted in [14] for the aging treatment.

3.5 Fatigue tests

The results of the fatigue tests are shown in Fig. 8a. Fitting curves corresponding to 50% (solid line), 10% and 90% (dashed lines enclosing a colored scatter band) failure probability, expressed by Eq. (2), are also plotted in Fig. 8a. The best-fit parameters and the standard deviation S are

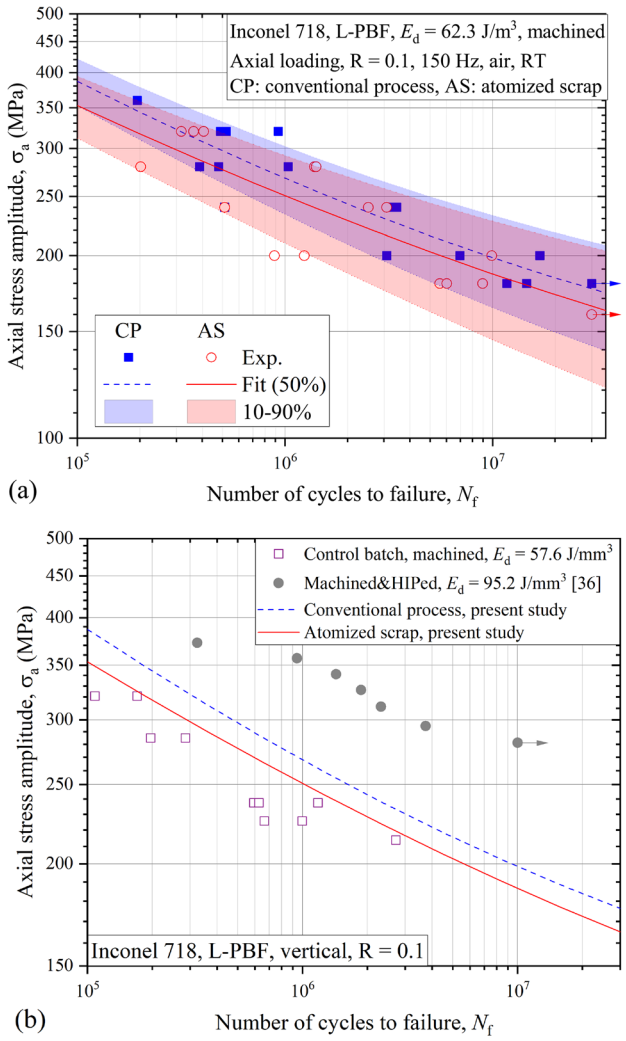

Fig. 8 **a** Results of the axial fatigue tests. Run-out tests are marked by arrows. **b** Comparison of the SN curves with data taken from the literature for HIPed variant [36] and with a control batch obtained on machined samples manufactured according to process parameters set in [14]

Table 5 Summary of Wohler curves and best-fit coefficients of Eq. (2) used to interpolate the HCF test results

Powder feedstock	c_1 (MPa)	c_2 (MPa)	c_3	Standard deviation, S (MPa)	$\sigma_{a,3\times10^7}$(MPa)
CP	101	4228	0.234	26.7	176
AS	79	2842	0.203	32.1	165

listed in Table 5, which also indicates the estimation of the fatigue strength at 3×10^7 cycles. It can be noted that the SN curves for both powder variants display a steadily declining trend with increasing number of cycles to failure, a behavior typically observed in additively manufactured metallic materials affected by internal defects [16]. In addition, both material variants display quite dispersed fatigue properties, as evidenced by a coefficient of variation in HCF strength at 3×10^7 cycles of over 15%, another distinctive characteristic of additively manufactured materials [34, 35]. Due to the significant scatter in the fatigue data, it is challenging to distinguish a substantial difference in fatigue behavior between the two variants. This is further demonstrated by the considerable overlap in the 10–90% scatter bands of the two materials. Specifically, the HCF strength at 3×10^7 cycles for the CP variant is only marginally higher than that of the AS counterpart, by a mere 7%. In Fig. 8b, the SN curves with a 50% failure probability are compared to the results of fatigue tests performed on the control batch CB and to data reported in literature [36] for specimens in the same testing conditions (vertical direction, machined surface, aged microstructure), but with the added treatment of Hot Isostatic Pressing (HIP). The investigated variants exhibit a SN trend that aligns with CB, and the fatigue behavior of all three conditions is significantly inferior to that of the HIPed counterpart. This is likely due to the presence of similar internal defects affecting the former three material conditions, which is conversely eliminated by the HIP treatment.

3.6 Fractographic analyses: the influence of defects on fatigue strength

The fracture surfaces of the fatigue specimens were carefully examined using scanning electron microscopy (SEM) to gain deeper insights into the role of internal defects. Representative fracture surfaces are depicted in Fig. 9a, b, c, and d for AS (a, b) and CP (c, d) specimens at low (a–c) and high magnification (b–d), respectively. In both cases, a defect, indicated by a red arrow and circumscribed by a dashed line, triggers the fatigue crack initiation. Typically, these initiation sites were situated near the outer surface, a consistent observation across multiple specimens. The size of these critical defects, referred to as the "killer pore," was quantified by measuring the square root of the pore area $\sqrt{area}$ for all the fatigued specimens. In general, isolated pores were identified (for example, as seen in Fig. 9b). In cases where multiple pores were in close proximity (as shown in Fig. 9d), they were treated as a single pore cluster in case the distance between their centroids was less than the $\sqrt{area}$ of the smaller defect [37].

Figure 10a illustrates the cumulative probability distributions of killer defect sizes identified on the fracture surfaces of all the fatigued specimens. It is evident that these two sets of data align closely with the right tail of the populations previously presented in Fig. 6a, which were determined through image analysis conducted on optical micrographs. Utilizing the statistics of the largest extreme value distribution on the killer defects, we arrive at an expected defect size that fairly closely corresponds to the one inferred from

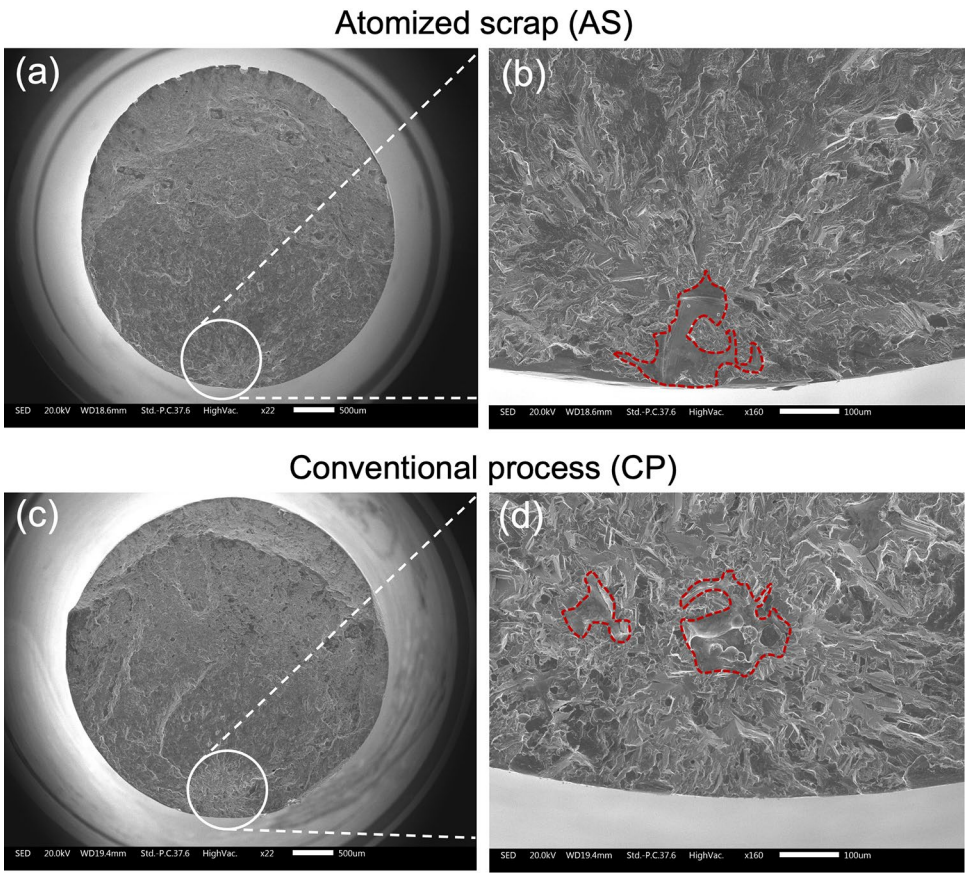

Fig. 9 SEM micrographs of the fracture surfaces around the fatigue crack initiation site. The defect responsible for crack nucleation is circumscribed by a dashed line. **a**, **b** Atomized scrap ($\sigma_a = 240$ MPa, $N_f = 5.1 \times 10^5$), **c**, **d** conventional process (($\sigma_a = 240$ MPa, $N_f = 3.2 \times 10^6$)

our analysis of optical micrographs. This congruence underscores the presence of larger defects in the AS variant.

Figure 10b displays the outcomes of the SN fatigue tests reanalyzed using a fracture mechanics approach. The best-fit coefficients for Eq. (6), which were used to model the data, are detailed in Table 6.

It is worth noting that both material variants exhibit nearly identical trends, and the scatter bands (as represented by colored bands in Fig. 10b) almost completely overlap. This significant finding underscores that the slight difference in fatigue strength can be primarily attributed to smaller critical defects in the CP compared to the AS variant, while the respective material's microstructure contributes little to variations in fatigue crack growth resistance between the two.

Indeed, it is intriguing that when we regard the high-cycle stress intensity factor range $\Delta K_{3\times10^7}$ (see Table 6) as an indicator of the material's crack growth threshold (ΔK_{th}), this value consistently stands at an approximate average value of 3.7 MPa$\sqrt{m}$.

Remarkably, this is in very good agreement with the short crack stress intensity threshold $\Delta K_{th,SC}$ evaluated according to El Haddad, Topper and Smit approach [38] then reformulated by Meneghetti et al. [39]:

$$\Delta K_{th,SC} = \Delta K_{th} \sqrt{\frac{Y^2\sqrt{area}}{Y^2\sqrt{area}+a_0}} \tag{7a}$$

$$a_0 = \frac{1}{\pi}\left(\frac{\Delta K_{th}}{\Delta \sigma_{lim}}\right)^2 \tag{7b}$$

In fact, using data documented in the literature for conventionally wrought Inconel 718 ($\Delta K_{th} = 4.0\text{MPa}\sqrt{\text{m}}$ [36, 40], $\Delta\sigma_{lim} = 560MPa$), a shape factor Y = 0.50, and an equivalent crack size $\sqrt{area}$ of 0.25 mm, viz. representative of the largest killer defect size found in the investigated material variants, a value of $\Delta K_{th,SC} = 3.7$ MPa$\sqrt{\text{m}}$ is obtained. This compelling correlation strongly reinforces the notion that utilizing powder feedstock from atomized scrap in the AS variant does not impact detrimentally on ductility and crack growth resistance of the material's matrix, which conversely proved to accommodate well the presence of rather large killer defects.

In conclusion, the fatigue properties, particularly in terms of crack growth resistance, and quasi-static properties of the AS condition closely match those achieved using conventional powder feedstock (both CP and CB conditions), all without necessitating specific adjustments to the processing

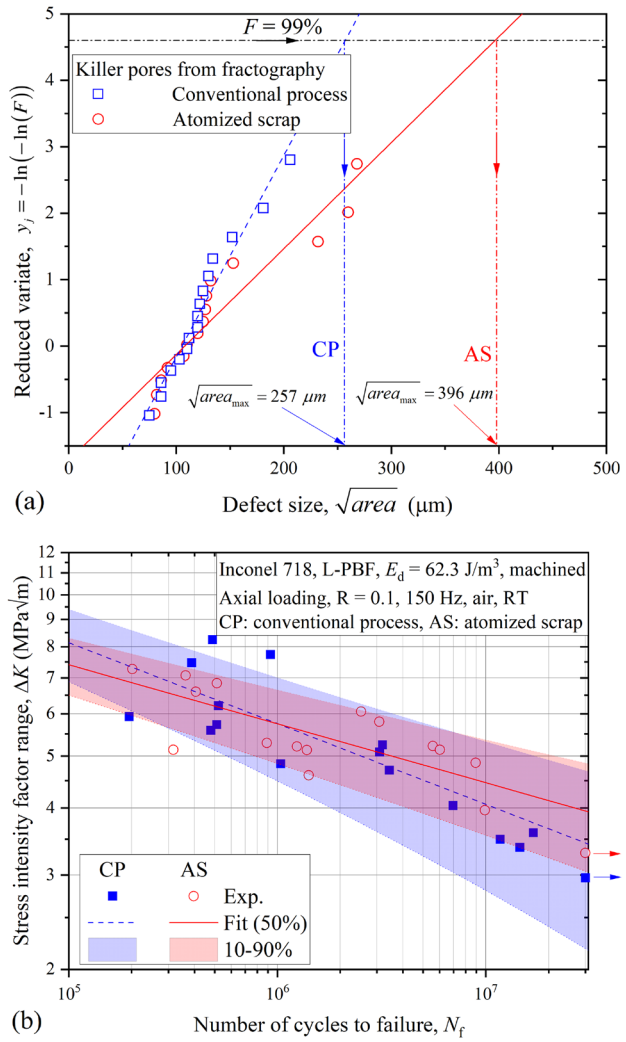

Fig. 10 **a** Cumulative probability distributions of the size of killer defects detected on the fracture surface of fatigued specimens. **b** SN fatigue data of Fig. 8a reanalyzed in terms of stress intensity factor range ΔK applied to the killer defect found in each fatigued specimen

Table 6 Best-fit coefficients of Eq. (6) used to interpolate the ΔK vs. N_f results

Powder feedstock	k_1 (MPa$\sqrt{m}$)	k_2	Standard deviation, S (MPa$\sqrt{m}$)	$\Delta K_{3\times10^7}$(MPa)
CP	46.2	0.151	0.98	3.44
AS	26.3	0.110	0.70	3.95

parameters. Nevertheless, it is crucial to acknowledge that the mechanical behavior is still influenced by the presence of internal defects. To attain even greater mechanical performance, ongoing efforts should focus on minimizing the size of these critical defects.

4 Conclusions

The present study explored the potential use of Inconel 718 powder feedstock generated via atomization of metallic scrap, and the results are promising. The life cycle assessments showed a remarkable reduction in energy consumption and carbon footprint by over 90% compared to conventionally produced powder, while also providing a sustainable source of critical raw materials like Ni. Moreover, microstructural, static, and fatigue analyses demonstrated that this secondary-source powder feedstock could achieve properties comparable to those of conventionally processed powders in terms of both ductility and fatigue strength, without the need for specific process parameter adjustments, unless even smaller critical defect sizes are required. Although additional research is required to evaluate the material's performance under impact loading and in notch fatigue scenarios, the findings suggest that Inconel 718 powder feedstock produced from secondary sources can be a feasible and eco-friendly alternative to conventionally produced powders.

Acknowledgements The experimental characterization performed by Mr. L. Festi and Mr. G. Stroili is gratefully acknowledged.

Author contributions All the authors contributed to the study conception and design. Material preparation, data collection and analysis were performed by MB, MP, GM and CM. MV and AG prepared the powder feedstock from metallic scrap. The first draft of the manuscript was written by MB, and all the authors commented on previous versions of the manuscript. All the authors read and approved the final manuscript.

Funding This work was financially supported by Italian Ministry of University and Research (MUR) in the frame of the programme "PNRR_Piano Nazionale di Ripresa e Resilienza", project title "PNRR_EI_iNEST_Spoke 3_ CUP E63C22001030007", grant number ECS_00000043.

Data availability Data available on request.

Declarations

Conflict of interest The authors have no relevant financial or non-financial interests to disclose.

References

1. Dhiman S, Joshi RS, Singh S, Gill SS, Singh H, Kumar R, Kumar V (2021) A framework for effective and clean conversion of machining waste into metal powder feedstock for additive manufacturing. Clean Eng Technol 4:100151. https://doi.org/10.1016/j.clet.2021.100151
2. Fullenwider B, Kiani P, Schoenung JM, Ma K (2019) Two-stage ball milling of recycled machining chips to create an alternative feedstock powder for metal additive manufacturing. Powder Technol 342:562–571. https://doi.org/10.1016/j.powtec.2018.10.023
3. Mahboubi Soufiani A, Enayati MH, Karimzadeh F (2010) Fabrication and characterization of nanostructured Ti6Al4V powder from machining scraps. Adv Powder Technol 21:336–340. https://doi.org/10.1016/j.apt.2009.12.018
4. Cacace S, Furlan V, Sorci R, Semeraro Q, Boccadoro M (2020) Using recycled material to produce gas-atomized metal powders for additive manufacturing processes. J Clean Prod 268:122218. https://doi.org/10.1016/j.jclepro.2020.122218
5. Moghimian P, Poirié T, Habibnejad-Korayem M, Zavala JA, Kroeger J, Marion F, Larouche F (2021) Metal powders in additive manufacturing: A review on reusability and recyclability of common titanium, nickel and aluminum alloys. Addit Manuf 43:102017. https://doi.org/10.1016/j.addma.2021.102017
6. Gruber K, Smolina I, Kasprowicz M, Kurzynowski T (2021) Evaluation of inconel 718 metallic powder to optimize the reuse of powder and to improve the performance and sustainability of the laser powder bed fusion (Lpbf) process. Materials (Basel) 14:1538. https://doi.org/10.3390/ma14061538
7. Cordova L, Campos M, Tinga T (2019) Revealing the effects of powder reuse for selective laser melting by powder characterization. Jom 71:1062–1072. https://doi.org/10.1007/s11837-018-3305-2
8. Ardila LC, Garciandia F, González-Díaz JB, Álvarez P, Echeverria A, Petite MM, Deffley R, Ochoa J (2014) Effect of IN718 recycled powder reuse on properties of parts manufactured by means of selective laser melting. Phys Proced 56:99–107. https://doi.org/10.1016/j.phpro.2014.08.152
9. Nandwana P, Peter WH, Dehoff RR, Lowe LE, Kirka MM, Medina F, Babu SS (2016) Recyclability study on Inconel 718 and Ti-6Al-4V powders for use in electron beam melting. Metall Mater Trans B 47:754–762. https://doi.org/10.1007/s11663-015-0477-9
10. Choi H, Kim S, Goto M, Kim S (2021) Effect of powder recycling on room and elevated temperature damage tolerability of Inconel 718 alloy fabricated by laser powder bed fusion. Mater Charact 171:110818. https://doi.org/10.1016/j.matchar.2020.110818
11. Tupac-Yupanqui H, Armani A (2021) Additive manufacturing of functional Inconel 718 parts from recycled materials. J Mater Eng Perform 30:1177–1187. https://doi.org/10.1007/s11665-020-05402-8
12. Palumbo E, Soust-Verdaguer B, Llatas C, Traverso M (2020) How to obtain accurate environmental impacts at early design stages in bim when using environmental product declaration. Method Support Decis-Mak Sustain 12:6927. https://doi.org/10.3390/su12176927
13. Huijbregts MAJ, Hellweg S, Frischknecht R, Hendriks HWM, Hungerbühler K, Hendriks AJ (2010) Cumulative energy demand as predictor for the environmental burden of commodity production. Environ Sci Technol 44:2189–2196. https://doi.org/10.1021/es902870s
14. Macoretta G, Bertini L, Monelli BD, Berto F (2022) Productivity-oriented SLM process parameters effect on the fatigue strength of Inconel 718. Int J Fatigue 168:107384. https://doi.org/10.1016/j.ijfatigue.2022.107384
15. Zhang D, Niu W, Cao X, Liu Z (2015) Effect of standard heat treatment on the microstructure and mechanical properties of selective laser melting manufactured Inconel 718 superalloy. Mater Sci Eng A 644:32–40. https://doi.org/10.1016/j.msea.2015.06.021
16. Benedetti M, Fontanari V, Bandini M, Zanini F, Carmignato S (2018) Low- and high-cycle fatigue resistance of Ti-6Al-4V ELI additively manufactured via selective laser melting: Mean stress and defect sensitivity. Int J Fatigue 107:96–109. https://doi.org/10.1016/j.ijfatigue.2017.10.021
17. Betriebsfestigkeit, Springer-Verlag, Berlin/Heidelberg (2006). https://doi.org/10.1007/3-540-29364-7
18. Murakami Y, Kodama S, Konuma S (1989) Quantitative evaluation of effects of non-metallic inclusions on fatigue strength of high strength steels. I: Basic fatigue mechanism and evaluation of correlation between the fatigue fracture stress and the size and location of non-metallic inclusions. Int J Fatigue 11:291–298. https://doi.org/10.1016/0142-1123(89)90054-6
19. Murakami Y (2002) Metal fatigue: effects of small defects and nonmetallic inclusions. Elsevier, Oxford
20. Strondl A, Lyckfeldt O, Brodin H, Ackelid U (2015) Characterization and control of powder properties for additive manufacturing. JOM 67:549–554. https://doi.org/10.1007/s11837-015-1304-0
21. Gruber H, Henriksson M, Hryha E, Nyborg L (2019) Effect of powder recycling in electron beam melting on the surface chemistry of alloy 718 powder. Metall Mater Trans A 50:4410–4422. https://doi.org/10.1007/s11661-019-05333-7
22. Jelis E, Clemente M, Kerwien S, Ravindra NM, Hespos MR (2015) Metallurgical and mechanical evaluation of 4340 steel produced by direct metal laser sintering. JOM 67:582–589. https://doi.org/10.1007/s11837-014-1273-8
23. Hosseini E, Popovich VA (2019) A review of mechanical properties of additively manufactured Inconel 718. Addit Manuf 30:100877. https://doi.org/10.1016/j.addma.2019.100877
24. Sindhura D, Sravya MV, Murthy GVS (2019) Comprehensive microstructural evaluation of precipitation in Inconel 718. Metallogr Microstruct Anal 8:233–240. https://doi.org/10.1007/s13632-018-00513-0
25. Huang J, Huang Z, Du H, Zhang J (2022) Effect of aging temperature on microstructure and tensile properties of Inconel 718 fabricated by selective laser melting. Trans Indian Inst Met 75:1403–1410. https://doi.org/10.1007/s12666-021-02487-0
26. Aydinöz ME, Brenne F, Schaper M, Schaak C, Tillmann W, Nellesen J, Niendorf T (2016) On the microstructural and mechanical properties of post-treated additively manufactured Inconel 718 superalloy under quasi-static and cyclic loading. Mater Sci Eng A 669:246–258. https://doi.org/10.1016/j.msea.2016.05.089
27. Godec M, Malej S, Feizpour D, Donik Č, Balažic M, Klobčar D, Pambaguian L, Conradi M, Kocijan A (2021) Hybrid additive manufacturing of Inconel 718 for future space applications. Mater Charact 172:110842. https://doi.org/10.1016/j.matchar.2020.110842
28. Al-Maharma AY, Patil SP, Markert B (2020) Effects of porosity on the mechanical properties of additively manufactured components: a critical review. Mater Res Express 7:122001. https://doi.org/10.1088/2053-1591/abcc5d
29. Li L (2006) Repair of directionally solidified superalloy GTD-111 by laser-engineered net shaping. J Mater Sci 41:7886–7893. https://doi.org/10.1007/s10853-006-0948-0
30. Murakami Y, Endo M (1994) Effects of defects, inclusions and inhomogeneities on fatigue strength. Int J Fatigue 16:163–182. https://doi.org/10.1016/0142-1123(94)90001-9
31. Beretta S, Murakami Y (1998) Statistical analysis of defects for fatigue strength prediction and quality control of materials. Fatigue Fract Eng Mater Struct 21:1049–1065. https://doi.org/10.1046/j.1460-2695.1998.00104.x

32. Solberg K, Wan D, Berto F (2020) Fatigue assessment of as-built and heat-treated Inconel 718 specimens produced by additive manufacturing including notch effects. Fatigue Fract Eng Mater Struct 43:2326–2336. https://doi.org/10.1111/ffe.13300
33. Chang L, Sun W, Cui Y, Zhang F, Yang R (2014) Effect of heat treatment on microstructure and mechanical properties of the hot-isostatic-pressed Inconel 718 powder compact. J Alloys Compd 590:227–232. https://doi.org/10.1016/j.jallcom.2013.12.107
34. Lewandowski JJ, Seifi M (2016) Metal additive manufacturing: a review of mechanical properties. Annu Rev Mater Res 46:151–186. https://doi.org/10.1146/annurev-matsci-070115-032024
35. Yamashita Y, Murakami T, Mihara R, Okada M, Murakami Y (2018) Defect analysis and fatigue design basis for Ni-based superalloy 718 manufactured by selective laser melting. Int J Fatigue 117:485–495. https://doi.org/10.1016/j.ijfatigue.2018.08.002
36. Witkin DB, Patel D, Albright TV, Bean GE, McLouth T (2020) Influence of surface conditions and specimen orientation on high cycle fatigue properties of Inconel 718 prepared by laser powder bed fusion. Int J Fatigue 132:105392. https://doi.org/10.1016/j.ijfatigue.2019.105392
37. Åman M, Okazaki S, Matsunaga H, Marquis GB, Remes H (2017) Interaction effect of adjacent small defects on the fatigue limit of a medium carbon steel. Fatigue Fract Eng Mater Struct 40:130–144. https://doi.org/10.1111/ffe.12482
38. El Haddad MH, Smith KN, Topper TH (1979) Fatigue crack propagation of short cracks. J Eng Mater Technol 101:42–46. https://doi.org/10.1115/1.3443647
39. Meneghetti G, Rigon D, Gennari C (2019) An analysis of defects influence on axial fatigue strength of maraging steel specimens produced by additive manufacturing. Int J Fatigue 118:54–64. https://doi.org/10.1016/j.ijfatigue.2018.08.034
40. Yuen JL, Roy P, Nix WD (1984) Effect of oxidation kinetics on the near threshold fatigue crack growth behavior of a nickel base superalloy. Metall Trans A 15:1769–1775. https://doi.org/10.1007/BF02666360